

Article

Analysis of Model Predictive Current-Controlled Permanent Magnet Synchronous Motor Drives with Inaccurate DC Bus Voltage Measurement

Wei Wang *  and Zhixiang Lu

School of Electrical Engineering, Southeast University, Nanjing 210096, China; luzhi401@foxmail.com

* Correspondence: wangwei1986@seu.edu.cn; Tel.: +86-025-8379-4169 (ext. 803)

Received: 3 December 2019; Accepted: 7 January 2020; Published: 10 January 2020



Abstract: In this paper, the effects of inaccurate DC bus voltage measurement are analyzed to model predictive current-controlled permanent magnet synchronous motor (PMSM) drives. It is found that the selection of the optimal space vector is affected by inaccurate DC bus voltage measurements, and the shortest distance principle is proposed to evaluate the effects. With the under-voltage measurement, the actual q axis current is always larger than the reference value, and PMSM may be damaged by the over-current phenomenon. However, the actual q axis current is always smaller than the reference value with the over-voltage measurement, and the rated torque capacity cannot be properly used. The effects of the over-voltage measurement are more serious than those of the under-voltage measurement. Additionally, the larger DC bus voltage measurement error can result in more serious effects than with the over-voltage measurement. Considering the limited variation range of the actual DC bus voltage, the rated value can be set as the measured value and the effects can be neglected. However, the effects should be taken into account if the variation range of the actual DC bus voltage is large. All the theoretical analyses are verified by experimental results.

Keywords: model predictive current control (MPCC); permanent-magnet synchronous motor (PMSM); DC bus voltage; shortest distance principle

1. Introduction

As a result of their high efficiency, high power density, and high torque-to-inertia ratio, permanent magnet synchronous motors (PMSMs) have been widely used recently [1–8]. Model predictive control (MPC) has recently attracted more attention because of its excellent performance aspects, such as its fast dynamic response, simple modeling, and multiconstraint control [9–15]. Based on the finite voltage vector set and the system model, MPC predicts the future behavior of control variables, such as the current, torque, and stator flux [12–14]. A cost function is designed according to the errors between the reference and predicted values, and the best voltage vector can be selected to minimize the cost function [15]. Compared with conventional direct torque control (DTC) and hysteresis current control (HCC), MPC performs better in multiobjective optimization of complicated drive systems, since a cost function is adopted [16–18]. Compared with the conventional proportional integral derivative (PID) control, model predictive current control (MPCC) has faster dynamic response, a lower current ratio, and fewer parameter adjustments, since no PID regulator is adopted [19,20]. Recently, artificial intelligence (AI) techniques, such as the artificial ant clustering technique, neural network algorithm, and fuzzy control method, have attracted more attention and have been successfully applied in fault diagnosis and motor modeling [21–23]. However, AI techniques have not been widely applied in motor drives, since they have heavy computation burden compared with MPC.

So far, various MPC formulations have been proposed for PMSM drives, and they can be mainly categorized into model predictive torque control (MPTC) [22] and model predictive current control (MPCC) [23]. In MPTC, torque and stator flux are selected as the control variables, and their errors are combined together to form a cost function. However, a weighting factor is required in the cost function, since both the torque and the stator flux have different units [24]. Additionally, the torque and the stator flux usually cannot be measured easily, and they are usually estimated by mathematical observers. In MPCC, the control variables are direct and quadrature axis currents, which can be measured by sensors directly. Furthermore, the weighting factor can be eliminated in MPCC, since both control variables have same units.

In order to predict future control variables of MPC, several input signals are required for the PMSM model. For example, the DC bus voltage is required to reconstruct voltage vectors, and it is usually measured by a voltage sensor in both MPTC and MPCC. However, the voltage sensor may experience static electricity corrosion, high humidity, high temperature, and mechanical vibration [25]. Hence, specific voltage sensor faults (VSFs) may occur, such as temperature drift, zero offset, gain variation, and signal loss [26–29]. As a result, the DC bus voltage measurement error will appear. In [30,31], the effects of inaccurate DC bus voltage in three-phase AC/DC converters are analyzed and voltage compensation strategies are proposed to solve the voltage mismatch. Several voltage observers are built to estimate the DC bus voltage [32–40]. In automotive systems, a nonlinear DC bus voltage observer was designed to deal with the information of real-time PWM cycles in both traction and charger modes [32]. One study [33] developed an adaptive observer for induction motor drives to estimate the DC bus voltage. Another study [32] proposed a fault-tolerant control scheme consisting of two higher order sliding mode observers and one Luenberger observer (LO) against VSFs. For PMSM drive systems, the model reference adaptive (MRA) method is adopted in [35,36] for online DC voltage identification. Compared with other observers, the MRA method is relatively easy to implement, while its estimation precision heavily depends on motor parameters [36]. In [37], a sliding-mode MRA observer is developed to quickly obtain accurate DC bus voltage values against motor parameter uncertainty and external disturbances.

Unfortunately, to the best of authors' knowledge, no existing literature has discussed the effects of inaccurate DC bus voltage measurement on MPCC-PMSM drives. The aim of this paper is to discuss these effects, which is the main contribution of this paper. This paper is organized as follows. The studied MPCC-PMSM drive is described in Section 2. The effects of the inaccurate DC bus voltage measurement on MPCC-PMSM are analyzed in Section 3. Experiments are carried out in Section 4 to verify the theoretical analysis. Finally, conclusions are drawn in Section 5.

2. Studied MPCC-PMSM Drive

The studied MPCC-PMSM drive system is illustrated in Figure 1, in which the surface-mounted PMSM is fed by a voltage source inverter (VSI). The DC bus voltage u_{DC} is measured by a voltage sensor. To simplify analysis, two assumptions are defined as follows:

- (1) The variations of both the electrical rotor position θ_e and the electrical angular speed ω_e of PMSM can be neglected in one sampling period T_s ;
- (2) The stator inductance L_s , the stator resistance R_s , and the permanent magnet flux ψ_{pm} remain unchanged during the entire operation.

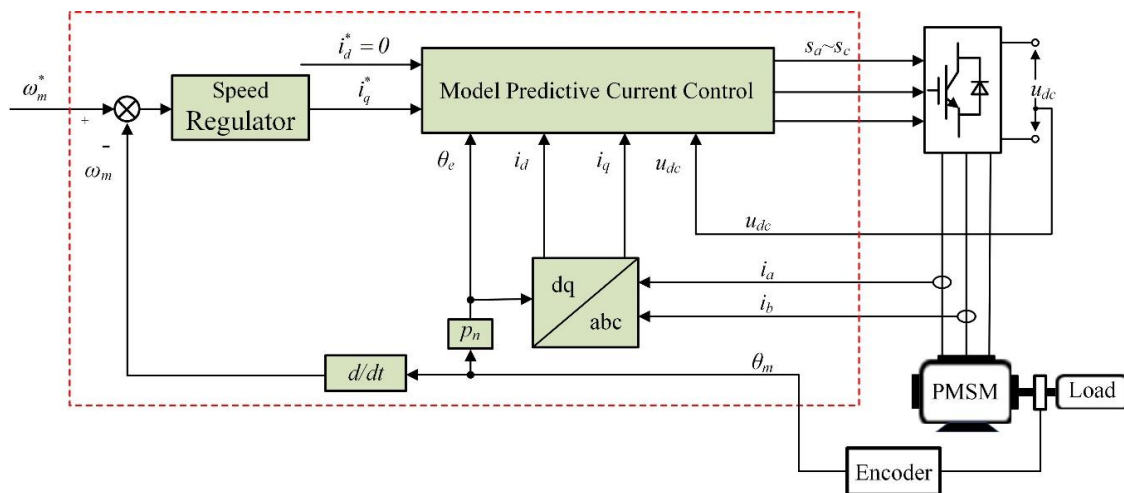


Figure 1. Studied model predictive current control permanent magnet synchronous motor (MPCC-PMSM) drive system.

2.1. Current Prediction

In this paper, d axis and q axis currents of the PMSM are chosen as control variables. The voltage equation of the PMSM in the d - q coordinate system can be established as

$$\begin{cases} u_d = R_s i_d + L_s di_d/dt - \omega_e L_q i_q \\ u_q = R_s i_q + L_s di_q/dt + \omega_e (L_d i_d + \psi_{pm}) \end{cases} \quad (1)$$

where $u_d, u_q, i_d,$ and i_q are voltages and currents in the d - q coordinate system. Considering the discrete time state–space model with a sampling period T_s , the current differential is

$$\frac{di(k)}{dt} \approx \frac{i(k+1) - i(k)}{T_s} \quad (2)$$

where $i(k)$ is the sensed current in the k th sampling period.

Substituting Equation (2) into Equation (1) gives

$$\begin{cases} i_d(k+1) = A i_d(k) + B i_q(k) + C u_d(k) \\ i_q(k+1) = -B i_d(k) + A i_q(k) + C u_q(k) - D_{pm} \end{cases} \quad (3)$$

with

$$A = 1 - R_s T_s / L_s, B = T_s \omega_e, C = T_s / L_s, D_{pm} = T_s \omega_e \varphi_{pm} / L_s \quad (4)$$

$$\begin{bmatrix} u_d(k) & u_q(k) \end{bmatrix}^T = T_{3s/2r} u_{dc}(k) [s_a \ s_b \ s_c]^T \quad (5)$$

where $T_{3s/2r}$ is the transformation matrix from the abc coordinate system to the d - q coordinate system; (s_a, s_b, s_c) is the space vector (SV) of the voltage source inverter (VSI) and the switch state s_x is defined as:

$$s_x = \begin{cases} 1 & \text{if } x\text{-th leg upper switch is ON} \\ 0 & \text{if } x\text{-th leg lower switch is ON} \end{cases} \quad (x = a, b, c) \quad (6)$$

All candidate SVs are listed in Table 1.

Table 1. Space vectors (SVs) of the MPCC.

SV	U_0	U_1	U_2	U_3	U_4	U_5	U_6	U_7
$s_a \ s_b \ s_c$	000	100	110	010	011	001	101	111

2.2. Cost Function

The cost function is designed to evaluate the performance of predicted currents. Usually, the deviation between the predicted value and reference value is considered. It is obvious that a smaller current deviation represents better performance of the corresponding SV. As a result, the cost function is designed as

$$J_n = [i_d^*(k+1) - i_{dn}(k+1)]^2 + [i_q^*(k+1) - i_{qn}(k+1)]^2, n=0,1,\dots,7 \quad (7)$$

which is designed to evaluate the deviation between the reference and predicted currents. A smaller cost function means less current tracking error and better performance. To acquire maximum torque per ampere (MTPA), the reference d axis current $i_d^*(k+1)$ is set as 0 and the reference q axis current $i_q^*(k+1)$ is the output of the speed regulator. The superscript n shows that the SV \mathbf{U}_n in Table 1 is used to calculate $i_{dn}(k+1)$, $i_{qn}(k+1)$, and J_n . The optimal SV \mathbf{U}_{op} is chosen to minimize cost function J_n

$$J_{op} = \min_{0 \leq n \leq 7} J_n \quad (8)$$

3. Effect Analysis

In this paper, the DC bus voltage measurement error Δu_{DC} is defined as the difference between the measured DC bus voltage u_{dc}^m and the actual value u_{DC} ; that is, $\Delta u_{DC} = u_{dc}^m - u_{DC}$. Three different measurements are defined as follows.

- (1) Accurate measurement: $\Delta u_{DC} = 0$;
- (2) Under-voltage measurement: $\Delta u_{DC} < 0$;
- (3) Over-voltage measurement: $\Delta u_{DC} > 0$;

Both the under-voltage and over-voltage measurements are also part of the inaccurate measurement. The effects of Δu_{DC} will be analyzed in this section.

3.1. Simplification of Cost Function

To simplify the analysis, the cost function (Equation (7)) is simplified in this subsection. According to Equations (3) and (4), the current prediction can be presented as

$$\begin{bmatrix} i_d(k+1) \\ i_q(k+1) \end{bmatrix} = \mathbf{P} \begin{bmatrix} i_d(k) \\ i_q(k) \end{bmatrix} + \mathbf{M} \begin{bmatrix} u_d(k) \\ u_q(k) \end{bmatrix} - \mathbf{Q} \quad (9)$$

with

$$\mathbf{P} = \begin{bmatrix} A & B \\ -B & A \end{bmatrix} \mathbf{M} = \begin{bmatrix} C & 0 \\ 0 & C \end{bmatrix} \mathbf{Q} = \begin{bmatrix} 0 \\ D_{pm} \end{bmatrix}$$

where d - and q axis voltages are expressed as

$$\begin{bmatrix} u_d(k) \\ u_q(k) \end{bmatrix} = \mathbf{M}^{-1} \left(\begin{bmatrix} i_d(k+1) \\ i_q(k+1) \end{bmatrix} - \mathbf{P} \begin{bmatrix} i_d(k) \\ i_q(k) \end{bmatrix} + \mathbf{Q} \right) \quad (10)$$

Substituting $i_d^*(k+1)$ and $i_q^*(k+1)$ into Equation (10) gives the reference d axis and q axis voltages u_d^* and u_q^* as

$$\begin{bmatrix} u_d^* \\ u_q^* \end{bmatrix} = \mathbf{M}^{-1} \left(\begin{bmatrix} i_d^*(k+1) \\ i_q^*(k+1) \end{bmatrix} - \mathbf{P} \begin{bmatrix} i_d(k) \\ i_q(k) \end{bmatrix} + \mathbf{Q} \right) \quad (11)$$

According to Equation (11), the reference voltage vector \mathbf{U}^* is mainly determined by u_q^* , since u_d^* is usually very small. Therefore, the effects of inaccurate measurement can be neglected for the d axis current. Comparing Equations (11) to (10), the voltage error can be calculated by

$$\begin{bmatrix} u_d^* - u_d(k) \\ u_q^* - u_q(k) \end{bmatrix} = \mathbf{M}^{-1} \begin{bmatrix} i_d^*(k+1) - i_d(k+1) \\ i_q^*(k+1) - i_q(k+1) \end{bmatrix} \quad (12)$$

According to Equation (12), Equation (7) can be simplified as

$$J_n = C\{[u_d^* - u_{dn}(k)]^2 + [u_q^* - u_{qn}(k)]^2\}, n = 0, 1 \dots 7 \quad (13)$$

where $u_{dn}(k)$ and $u_{qn}(k)$ are the d axis and q axis voltages calculated from the SV \mathbf{U}_n .

Considering the transformation between d-q and α - β coordinate systems, then

$$\begin{bmatrix} u_d \\ u_q \end{bmatrix} = \begin{bmatrix} \sin \theta_e & \cos \theta_e \\ -\cos \theta_e & \sin \theta_e \end{bmatrix} \begin{bmatrix} u_\alpha \\ u_\beta \end{bmatrix} \quad (14)$$

Substituting Equation (14) into Equation (13) gives

$$J_n = C[(u_\alpha^* - u_{\alpha n})^2 + (u_\beta^* - u_{\beta n})^2], n = 0, 1 \dots 7 \quad (15)$$

where u_α^* and u_β^* are the reference α axis and β axis voltages, respectively; $u_{\alpha n}$ and $u_{\beta n}$ are α axis and β axis voltages of \mathbf{U}_n , respectively.

The initial cost function (Equation (7)) consists of the measurement errors between reference and predictive currents. However, the simplified method (Equation (15)) adopts the measurement errors between reference and predictive α - β axis voltages. If u_α^* and u_β^* can be implemented ($u_\alpha^* = u_{\alpha n}$ and $u_\beta^* = u_{\beta n}$), the cost function J_n will be minimized to zero. According to Table 2, however, the number of candidate SVs is only eight, and u_α^* and u_β^* usually cannot be realized. The minimization of Equation (15) acts to find the nearest SV $[u_{\alpha n}, u_{\beta n}]$ to the reference voltage vector $[u_\alpha^* \ u_\beta^*]$.

Table 2. SVs in the α - β coordinate system.

SV	$u_\alpha + ju_\beta$
\mathbf{U}_0	0
\mathbf{U}_1	$2/3 u_{DC}$
\mathbf{U}_2	$(1/3 + j\sqrt{3}/3) u_{DC}$
\mathbf{U}_3	$(-1/3 + j\sqrt{3}/3) u_{DC}$
\mathbf{U}_4	$-2/3 u_{DC}$
\mathbf{U}_5	$(-1/3 - j\sqrt{3}/3) u_{DC}$
\mathbf{U}_6	$(1/3 - j\sqrt{3}/3) u_{DC}$
\mathbf{U}_7	0

The distance of \mathbf{U}_n is defined as L_n , which can be calculated by

$$L_n = \sqrt{(u_\alpha^* - u_{\alpha n})^2 + (u_\beta^* - u_{\beta n})^2}, n = 0, 1 \dots 7 \quad (16)$$

Considering both Equations (15) and (16), the optimal SV \mathbf{U}_{op} should have the shortest distance, which is defined as the shortest distance principle in this paper. According to the shortest distance principle, the distribution of the reference voltage vector \mathbf{U}^* can be divided into seven sectors (Sectors 0–6), as illustrated in Figure 2. In Sector n , the optimal SV is \mathbf{U}_n . For example, when \mathbf{U}^* is located in point Q1, as shown in Figure 2, \mathbf{U}_3 is selected as the optimal SV. A central hexagon with a radial length of $1/3u_{DC}$ is defined as Sector 0, and a zero SV is chosen by the minimum switching

actions principle. For example, \mathbf{U}_0 or \mathbf{U}_7 should be selected as the optimal SVs for point Q2, as shown in Figure 2.

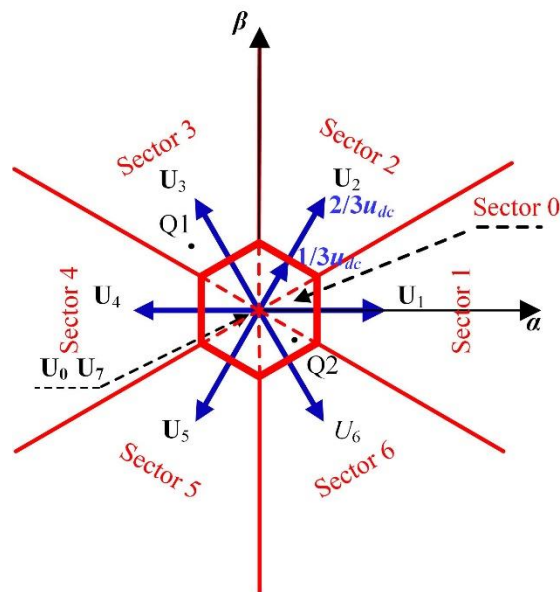


Figure 2. Distribution of reference voltage vector with accurate measurement.

3.2. Under-Voltage Measurement

With the under-voltage measurement, the distributions of the reference voltage vector \mathbf{U}^* for both u_{dc}^m and u_{DC} are illustrated in Figure 3, in which the affected zone is highlighted in green, while the non-affected zones are white.

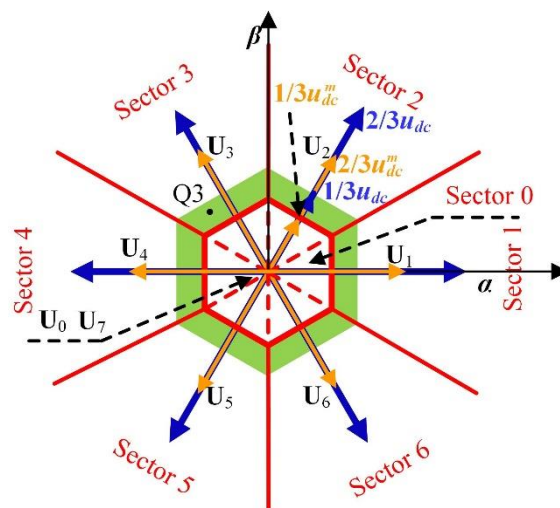


Figure 3. Distribution of reference voltage vector with under-voltage measurement.

To evaluate the effect, the priority of \mathbf{U}_n is defined as

$$H_n = \sum_{k=0}^6 (L_n \geq L_k) \quad n = 0, 1, \dots, 6 \quad (17)$$

According to Equation (17), \mathbf{U}_n is defined as the $(H_n)^{th}$ optimal SV. Obviously, smaller H_n means that \mathbf{U}_n is better for minimizing the cost function. Especially, \mathbf{U}_n is considered as the first optimal SV

\mathbf{U}_{op} if $H_n = 1$. It should be emphasized that the priority is determined according to the actual DC bus voltage u_{DC} in this paper, regardless of whether the DC bus voltage measurement error exists.

If the first optimal SV is determined by u_{dc}^m , however, its priority may be not 1, since the DC bus voltage measurement error exists. To differ from the actual first optimal SV, the first optimal SV determined by u_{dc}^m is defined as the pseudo first optimal SV in this paper. According to the priority of the pseudo first optimal SV, the whole distribution of the reference voltage vector is divided into two zones, as shown in A-1 (white) and A-2 (green) in Figure 3. The priorities of the pseudo first optimal SVs in A-1 and A-2 are 1 and 2, respectively. Obviously, A-2 (green) is the affected zone. If the reference voltage vector \mathbf{U}^* is located in A-2 (green), the selected SV is the first optimal one for u_{dc}^m , but the second optimal one for u_{DC} . In fact, the first optimal SV for u_{DC} should be a zero SV instead of an active one. Compared with the accurate measurement, more active SVs are selected in the under-voltage measurement. Therefore, the actual q axis current i_q is always larger than the reference value i_q^* . However, the difference between i_q and i_q^* is usually small, since the second optimal SV in the affected zone also can be considered as a good selection.

3.3. Over-Voltage Measurement

With the over-voltage measurement, the distributions of the reference voltage vector \mathbf{U}^* for u_{dc}^m and u_{DC} are illustrated in Figure 4. Compared with Figure 3, a new affected zone A-3 (blue) appears in Figure 4, in which the priority of the pseudo first optimal SV is 3. Taking the point Q4 shown in Figure 4 as an example, the zero SV is the first optimal SV for u_{dc}^m , but the third optimal SV for u_{DC} . In fact, the first optimal SV for u_{DC} is an active SV, but it is replaced by a zero SV for u_{dc}^m in the affected zone. Therefore, less active SVs are selected, and the actual q axis current i_q is always smaller than the reference value i_q^* .

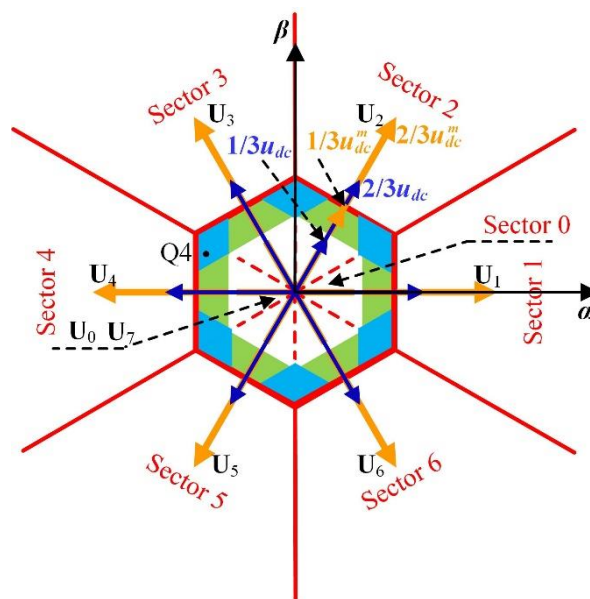


Figure 4. Distribution of reference voltage vector with over-voltage measurement.

Due to the existence of A-3 (blue), the effect of the over-voltage measurement is more serious than that of the under-voltage measurement. It can be found that affected zones A-2 and A-3 are restricted in the hexagon ring. The area proportions of A-2 (green) and A-3 (blue) in the hexagon ring vary with the voltage ratio γ ($\gamma = u_{dc}^m/u_{DC}$), as shown in Figure 5. It can be seen that the area proportion of A-3 is increased with the increase of γ . Therefore, the effect will become more serious with a higher voltage ratio γ . It should be emphasized that the value range of γ depends on the characteristics of the voltage sensor and system requirements. Usually, there is a range of DC bus voltage changes in

normal operations according to the system requirements. For example, the DC bus voltage of a subway traction system usually varies from 1200 V to 1800 V, while the rated value is 1500 V.

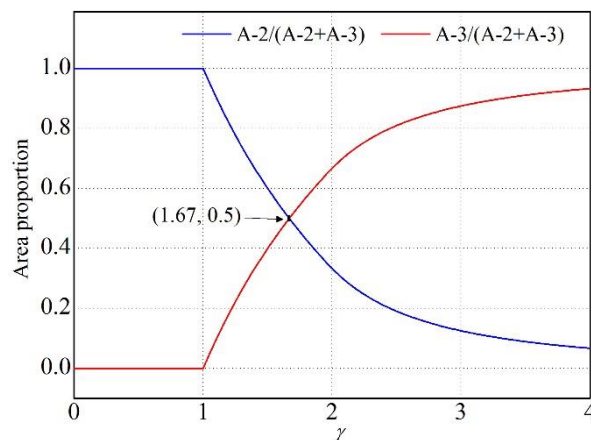


Figure 5. Area proportions of A-2 and A-3 for γ .

3.4. Reliability Analysis

In this paper, both A-1 (white) and A-2 (green) are defined as reliable zones, and A-3 (blue) is defined as the unreliable zone. With the under-voltage measurement, all zones are reliable, as shown in Figure 3. With the over-voltage measurement, however, the unreliable zone will appear, as shown in Figure 4, and it will be increased with the increase of γ , as shown in Figure 5. Usually, γ is very close to 1, and the unreliable zone is very small, as shown in Figure 5. However, γ may be far from 1 once the voltage sensor fails. In this situation, the MPCC will be affected if u_{dc}^m is still used in the current prediction. Fortunately, the actual DC bus voltage cannot significantly differ from the rated value in normal operations, which is the system requirement. For example, the DC bus voltage of a subway traction system usually varies from 1200 V to 1800 V, while the rated value is 1500 V. Hence, the measured DC bus voltage can be replaced with the rated value if their difference is very large. Therefore, the unreliable zone can be neglected for MPCC.

Even though the unreliable zone is small, it is still possible to locate the reference voltage vector \mathbf{U}^* in A-3. The position of the reference voltage vector \mathbf{U}^* depends on the synchronous current tracking errors, which cannot be too large; otherwise, \mathbf{U}^* will move into the reliable zone, since the unreliable zone is surrounded by the reliable zone in two directions (inside and outside, shown in Figure 4).

3.5. Effects of Sampling Period

The effects of the sampling period are evaluated for MPCC in this subsection. As is well known, the current ripples will deteriorate with a longer sampling period. On the other hand, the longer sampling period will reduce the average value of \mathbf{U}^* , and it is more likely to be located in A-2 and A-3 zones. As a result, the static current error will become larger, which is verified by simulation results in Figure 6. Simulation parameters of PMSM are shown in Table 3, and the speed command is set to 400 r/min. The nominal value of the DC bus voltage is set to 300 V. In simulation validation, the u_{dc}^m is set to 100 V, u_{DC} , and 500 V with different sampling periods, respectively. Obviously, the static current error can be reduced by increasing the sampling frequency. However, the sampling frequency sometimes is limited by the system features.

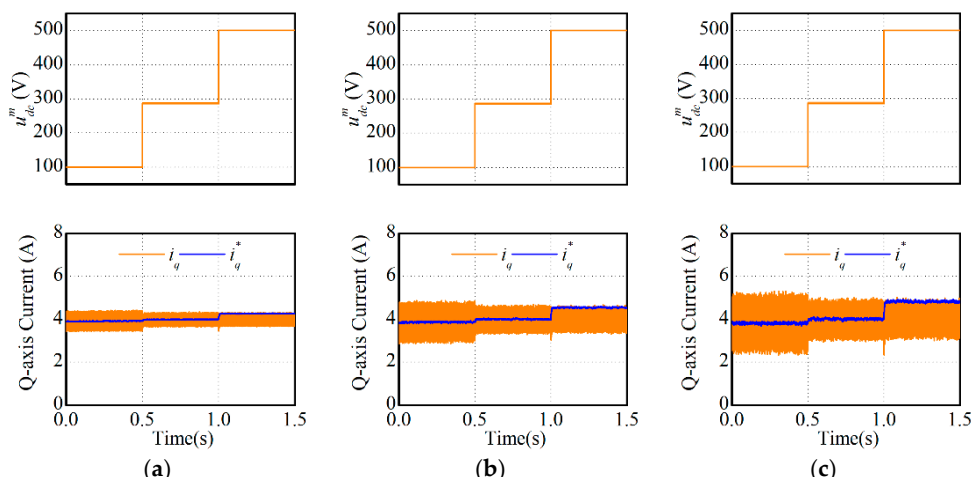


Figure 6. Simulation results of steady-state performance with sampling periods of (a) 25 μ s, (b) 50 μ s, and (c) 75 μ s.

Table 3. Parameters of a traction permanent magnet synchronous motor (PMSM).

Parameter	Value
Rated phase current	10 A
Stator resistance R_s	0.65 Ω
Stator inductance L_s	7.9 mH
Permanent magnet flux ψ_{PM}	0.41 Wb
Number of pole pairs P_n	4

4. Experimental Validation

To verify the effectiveness of the theoretical analysis, an experiment platform is developed, as shown in Figure 7. The traction PMSM is controlled by one three-leg VSI and its parameters are listed in Table 3. The load is provided by one PMSM with an encoder of 1024 pulses per revolution. The load is realized by the closed-loop torque control of the load PMSM by using field-oriented control (FOC). The control program is implemented in a dSPACE DS1103 controller. The inputs for the dSPACE DS1103 controller are the measured line currents and the DC bus voltage, as well as the feedback signal of the encoder. The switch states for the VSI are generated by the dSPACE DS1103 controller. A personal computer is employed to edit the control program and command the dSPACE DS1103 controller. The sampling frequency is 20 kHz. The nominal value of the DC bus voltage is 300 V, which is provided by a three-phase rectifier. The speed controller is realized by a proportion-integration (PI) regulator, in which the coefficients of proportional and integral parts are set to 0.05 and 0.2, respectively.

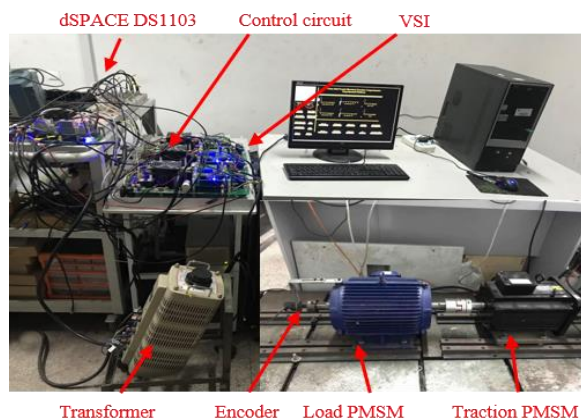


Figure 7. Experimental platform. Note: VSI = voltage source inverter.

4.1. Steady-State Operation

Steady-state performances with different measurements are provided in this experiment, in which the speed is 800 r/min and the measured DC bus voltage varies from 100 V to 800 V. The experimental results are illustrated in Figure 8 and are divided into six stages, including two under-voltage measurement stages (stage 1: 100 V; stage 2: 200 V), one accurate measurement stage (stage 3), and three over-voltage measurement stages (stage 4: 400 V; stage 5: 600 V; stage 6: 800 V).

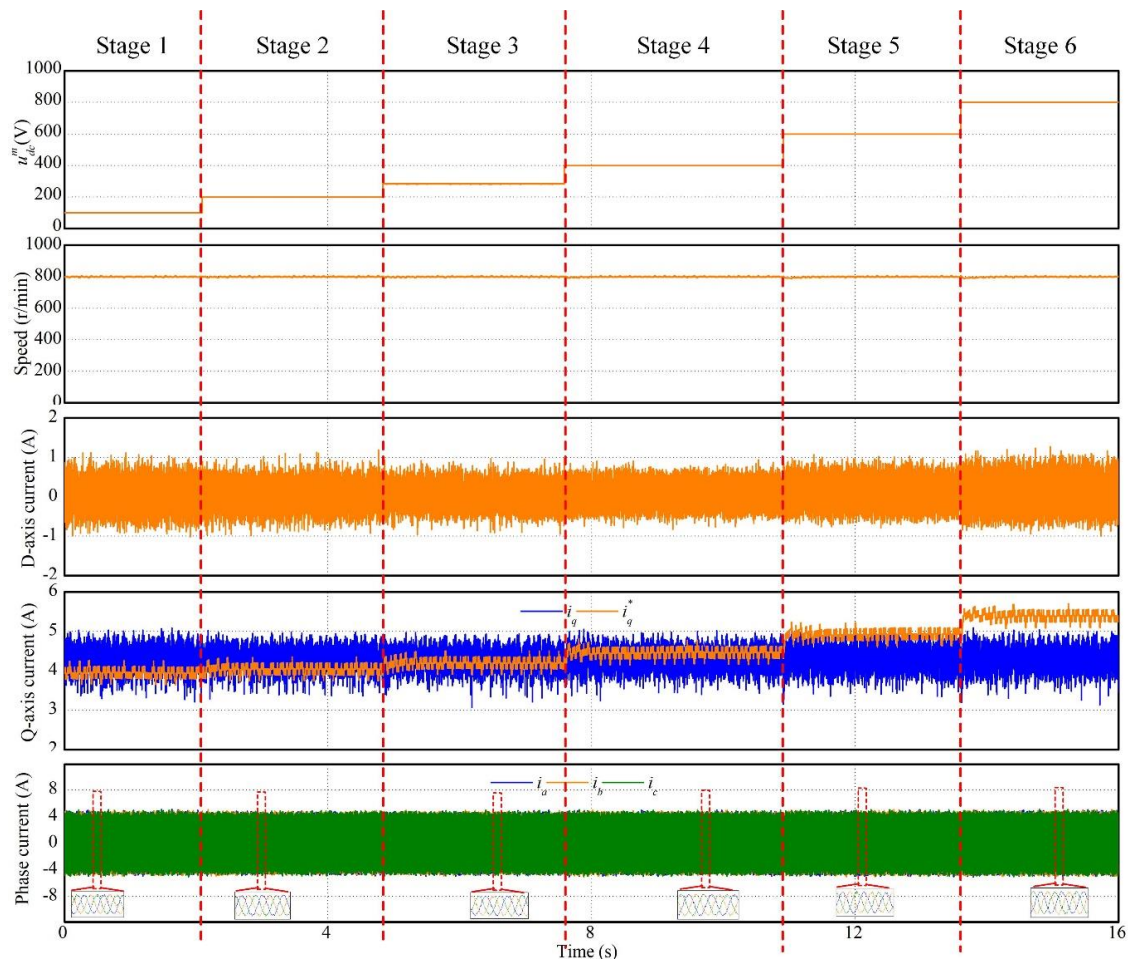


Figure 8. Steady-state performance with DC bus voltage measurement errors.

As shown in Figure 8, the actual currents are almost not affected by the DC bus voltage measurement errors in the steady-state operation. However, the reference q axis current is affected by the DC bus voltage measurement errors, and this effect becomes more serious when the DC bus voltage measurement error is larger. It can be found that reference q axis current is smaller than the actual value in the under-voltage measurement, while it is larger than the actual current in the over-voltage measurement.

The average current deviation Δi_q of the steady-state operation is defined as

$$\Delta i_q = \frac{1}{N} \sum_{k=1}^N [i_q^*(k) - i_q(k)] \quad (18)$$

The Δi_q values with different u_{dc}^m in steady-state operation are shown in Figure 9. As shown in Figure 9, the values of the current errors are very small, and their polarities are symmetrical for over-voltage error and under-voltage error.

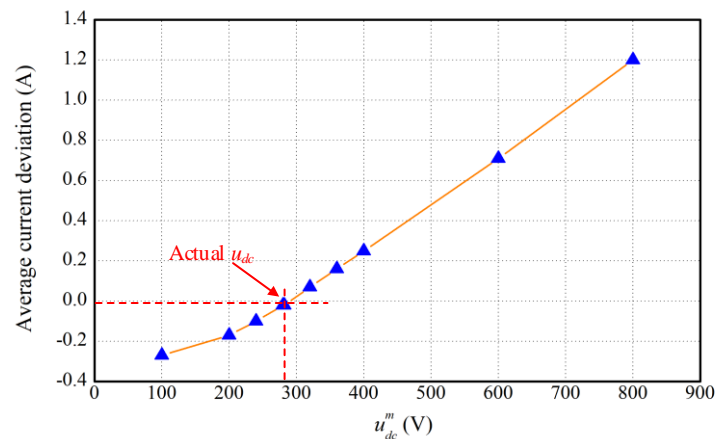


Figure 9. The Δi_q values with different u_{dc}^m in steady-state operation.

4.2. Torque Response

In this experiment, the speed command is set to 800 r/min and the torque command T_e^* changes from -20 Nm to 20 Nm, and then returns to -20 Nm. The measured DC bus voltages with the under-voltage and over-voltage measurements are set to 100 V and 500 V, respectively. The experimental results are illustrated in Figure 10. It can be seen in Figure 10 that MPCC has the same torque response for three different measurements. This can be explained as follows. According to Equation (12), the magnitude of the reference voltage vector \mathbf{U}^* is large during the torque response procedure. Therefore, \mathbf{U}^* is rarely located in the affected zone.

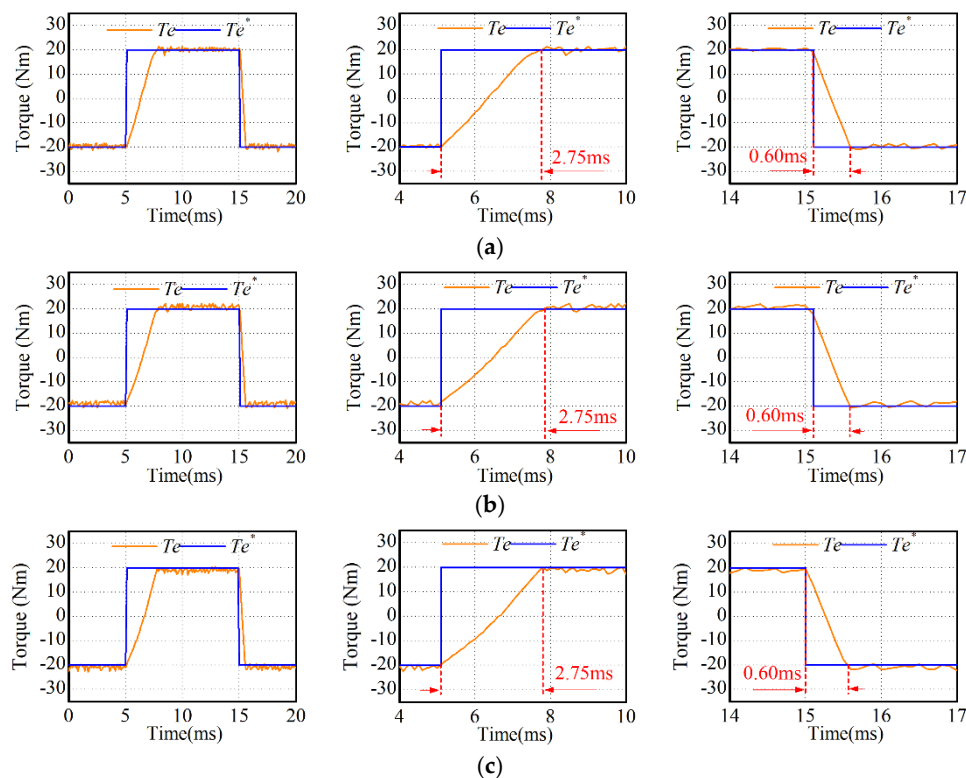


Figure 10. Torque response performances for (a) accurate measurement, (b) under-voltage measurement, and (c) over-voltage measurement.

4.3. Speed Response

In this experiment, the speed command changes from 200 r/min to 800 r/min, and then returns to 200 r/min. The measured DC bus voltages with the under-voltage and over-voltage measurements are also set to 100 V and 500 V, respectively. The experimental results are illustrated in Figures 11–13. It can be seen that the speed response performances are nearly not affected by the DC bus voltage measurement errors.

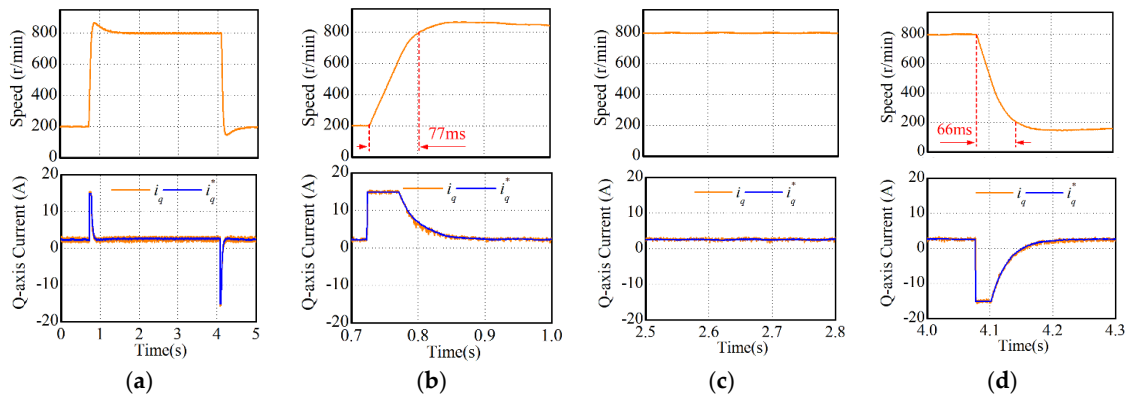


Figure 11. Speed response with accurate measurement: (a) 0–5 s, (b) 0.7–1.0 s, (c) 2.5–2.8 s, (d) 4.0–4.3 s.

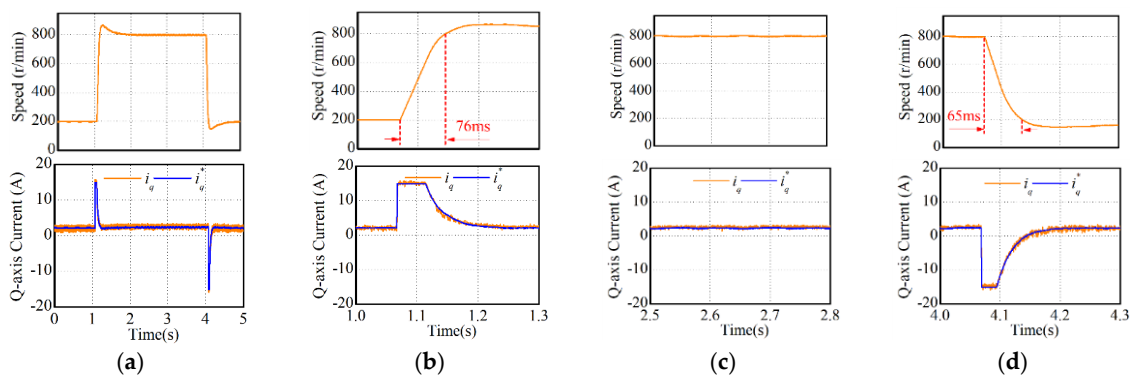


Figure 12. Speed response with under-voltage measurement (a) 0–5 s, (b) 1.0–1.3 s, (c) 2.5–2.8 s, (d) 4.0–4.3 s.

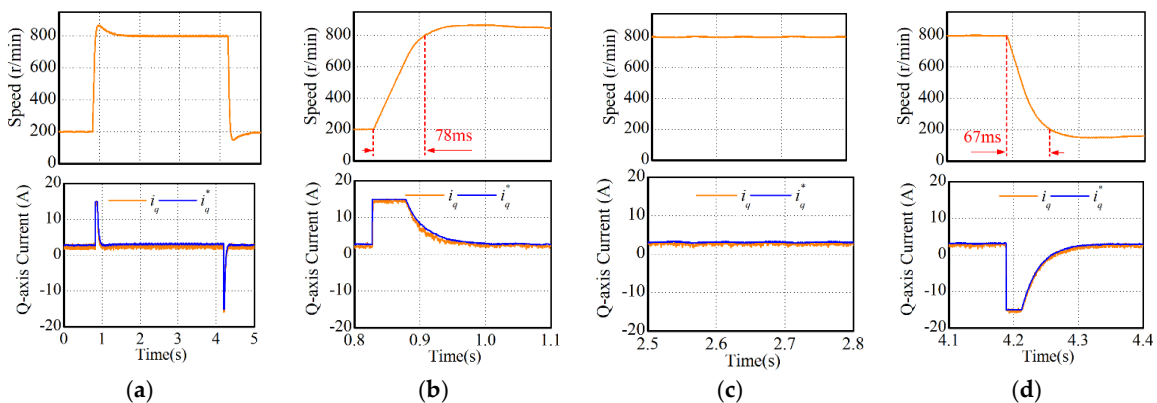


Figure 13. Speed response with over-voltage measurement: (a) 0–5 s, (b) 0.8–1.1 s, (c) 2.5–2.8 s, (d) 4.1–4.4 s.

5. Conclusions

Based on the shortest distance principle, the effects of the DC bus voltage measurement error are analyzed for MPCC-PMSM drives in this paper. It is found that the actual currents are almost not affected, but the effects of the reference q axis current are different with inaccurate measurements:

- (1) With the under-voltage measurement, the actual q axis current is always larger than the reference one, and the MPCC-PMSM drive may be damaged by the over-current phenomenon.
- (2) With the over-voltage measurement, the actual q axis current is always smaller than the reference one, and the normal torque capacity cannot be utilized.

For the purpose of safety, the variation range of the actual DC bus voltage is usually limited. Therefore, current deviations are usually very small and can be neglected. In fact, MPCC cannot perform adequately for some measurement errors, such as the measurement errors of phase currents and rotor positions. Usually, the performance of the MPCC will be affected by these measurement errors. However, the effects of these measurement errors are not the aim of this paper, so they are not discussed here. On the other hand, the serious measurement error of the DC bus voltage can be easily detected by comparing this with the normal variation range of the DC bus voltage. If the variation range of the DC bus voltage is large, it is suggested to replace the measured DC bus voltage with the rated value.

Author Contributions: Conceptualization, W.W.; methodology, W.W. and Z.L.; validation, Z.L.; resources, W.W. and Z.L.; writing—original draft preparation, W.W. and Z.L.; writing—review and editing, W.W. All authors have read and agreed to the published version of the manuscript.

Funding: This work was supported in part by National Natural Science Foundation of China (Project: 51977036 and 51607038) and ZhiShan Young Scholar Plan of Southeast University of China (Project: 2242019R40043).

Conflicts of Interest: The authors declare no conflict of interest.

References

1. Cheng, M.; Hua, W.; Zhang, J.; Zhao, W. Overview of stator-permanent magnet brushless machines. *IEEE Trans. Ind. Electron.* **2011**, *58*, 5087–5101. [[CrossRef](#)]
2. Chaoui, H.; Khayamy, M.; Okoye, O.; Gualous, H. Simplified speed control of permanent magnet synchronous motors using genetic algorithms. *IEEE Trans. Power Electron.* **2019**, *34*, 3563–3574. [[CrossRef](#)]
3. Lu, H.; Li, J.; Qu, R.; Ye, D.; Lu, Y. Fault-tolerant predictive control of six-phase PMSM drives based on pulsewidth modulation. *IEEE Trans. Ind. Electron.* **2019**, *66*, 4992–5003. [[CrossRef](#)]
4. Feng, G.; Lai, C.; Kar, N. A closed-loop fuzzy logic based current controller for PMSM torque ripple minimization using the magnitude of speed harmonic as the feedback control signal. *IEEE Trans. Ind. Electron.* **2017**, *64*, 2642–2653. [[CrossRef](#)]
5. Wang, W.; Feng, Y.; Shi, Y.; Cheng, M.; Hua, W. Direct thrust force control of primary permanent-magnet linear motors with single DC-link current sensor for subway applications. *IEEE Trans. Power Electron.* **2020**, *35*, 1365–1376. [[CrossRef](#)]
6. Pulvirenti, M.; Scarcella, G.; Scelba, G.; Testa, A.; Harbaugh, M. On-line stator resistance and permanent magnet flux linkage identification on open-end winding PMSM drives. *IEEE Trans. Ind. Appl.* **2019**, *55*, 504–515. [[CrossRef](#)]
7. Yamazaki, K.; Togashi, Y.; Ikemi, T.; Ohki, S.; Mizokami, R. Reduction of inverter carrier harmonic losses in interior permanent magnet synchronous motors by optimizing rotor and stator shapes. *IEEE Trans. Ind. Appl.* **2019**, *55*, 306–315. [[CrossRef](#)]
8. Wang, W.; Feng, Y.; Shi, Y.; Cheng, M.; Hua, W.; Wang, Z. Fault-tolerant control of primary permanent-magnet linear motors with single phase current sensor for subway applications. *IEEE Trans. Power Electron.* **2019**, *34*, 10546–10556. [[CrossRef](#)]
9. Yan, L.; Dou, M.; Hua, Z.; Zhang, H.; Yang, J. Robustness improvement of FCS-MPTC for induction machine drives using disturbance feedforward compensation technique. *IEEE Trans. Power Electron.* **2019**, *34*, 2874–2886. [[CrossRef](#)]

10. Sun, T.; Wang, J.; Griffo, A.; Sen, B. Active thermal management for interior permanent magnet synchronous machine (IPMSM) drives based on model predictive control. *IEEE Trans. Ind. Appl.* **2018**, *54*, 4506–4514. [[CrossRef](#)]
11. Wang, W.; Lu, Z.; Hua, W.; Wang, Z.; Cheng, M. Simplified model predictive current control of primary permanent-magnet linear motor traction systems for subway applications. *Energies* **2019**, *12*, 4144. [[CrossRef](#)]
12. Ram'irez, R.; Espinoza, J.; Villarroel, F.; Maurelia, E. A novel hybrid finite control set model predictive control scheme with reduced switching. *IEEE Trans. Ind. Electron.* **2014**, *61*, 5912–5920. [[CrossRef](#)]
13. Nguyen, H.; Jung, J. Finite control set model predictive control to guarantee stability and robustness for surface-mounted PM synchronous motors. *IEEE Trans. Ind. Electron.* **2018**, *65*, 8510–8519. [[CrossRef](#)]
14. Nguyen, H.; Jung, J. Asymptotic stability constraints for direct horizon-one model predictive control of SPMSM drives. *IEEE Trans. Power Electron.* **2018**, *33*, 8213–8219. [[CrossRef](#)]
15. Wang, W.; Zhang, J.; Cheng, M. Common model predictive control for permanent-magnet synchronous machine drives considering single-phase open-circuit fault. *IEEE Trans. Power Electron.* **2017**, *32*, 5862–5872. [[CrossRef](#)]
16. Lim, C.; Rahim, N.; Hew, W.; Levi, E. Model predictive control of a two-motor drive with five-leg-inverter supply. *IEEE Trans. Power Electron.* **2013**, *60*, 54–65. [[CrossRef](#)]
17. Wang, W.; Zhang, J.; Cheng, M.; Cao, R. Direct torque control of five-leg dual-PMSM drive systems for fault-tolerant purposes. *J. Power Electron.* **2017**, *17*, 161–171. [[CrossRef](#)]
18. Wang, W.; Zhang, J.; Cheng, M. A dual-level hysteresis current control for one five-leg VSI to control two PMSMs. *IEEE Trans. Power Electron.* **2017**, *32*, 804–814. [[CrossRef](#)]
19. Lim, C.; Levi, E.; Jones, M.; Rahim, N.; Hew, W. FCS-MPC-based current control of a five-phase induction motor and its comparison with PI-PWM control. *IEEE Trans. Ind. Electron.* **2014**, *61*, 149–163. [[CrossRef](#)]
20. Lin-Shi, X.; Morel, F.; Llor, A.; Allard, B.; Retif, J. Implementation of hybrid control for motor drives. *IEEE Trans. Ind. Electron.* **2007**, *54*, 1946–1952. [[CrossRef](#)]
21. Nyanteh, Y.; Edrington, C.; Sricastava, S.; Cartes, D. Application of artificial intelligence to real-time fault detection in permanent-magnet synchronous machines. *IEEE Trans. Ind. Appl.* **2013**, *49*, 1205–1214. [[CrossRef](#)]
22. Guo, Y.; Si, J.; Gao, C.; Feng, H.; Gan, C. Improved fuzzy-based Taguchi method for multi-objective optimization of direct-drive permanent magnet synchronous motors. *IEEE Trans. Magn.* **2019**, *55*, 1–4. [[CrossRef](#)]
23. Soualhi, A.; Clerc, G.; Razik, H. Detection and diagnosis of faults in induction motor using an improved artificial ant clustering technique. *IEEE Trans. Ind. Electron.* **2013**, *60*, 4053–4062. [[CrossRef](#)]
24. Zhang, X.; Zhang, L.; Zhang, Y. Model predictive current control for PMSM drives with parameter robustness improvement. *IEEE Trans. Power Electron.* **2019**, *34*, 1645–1657. [[CrossRef](#)]
25. Zhou, Z.; Xia, C.; Yan, Y.; Wang, Z.; Shi, T. Torque ripple minimization of predictive torque control for PMSM with extended control set. *IEEE Trans. Ind. Electron.* **2017**, *64*, 6930–6939. [[CrossRef](#)]
26. Zhang, C.; Wu, G.; Rong, F.; Feng, J.; Jia, L.; He, J.; Huang, S. Robust fault-tolerant predictive current control for permanent magnet synchronous motors considering demagnetization fault. *IEEE Trans. Ind. Electron.* **2018**, *65*, 5324–5334. [[CrossRef](#)]
27. Karamanakos, P.; Geyer, T. Model predictive torque and flux control minimizing current distortions. *IEEE Trans. Power Electron.* **2019**, *34*, 2007–2012. [[CrossRef](#)]
28. Zhang, K.; Jiang, B.; Yan, X.; Mao, Z. Incipient voltage sensor fault isolation for rectifier in railway electrical traction systems. *IEEE Trans. Ind. Electron.* **2017**, *64*, 6763–6774. [[CrossRef](#)]
29. Wu, C.; Guo, C.; Xie, Z.; Ni, F.; Liu, H. A signal-based fault detection and tolerance control method of current sensor for PMSM drive. *IEEE Trans. Ind. Electron.* **2018**, *65*, 9646–9657. [[CrossRef](#)]
30. Trinh, Q.; Wang, P.; Tang, Y. Compensation of DC offset and scaling errors in voltage and current measurements of three-phase AC/DC converters. *IEEE Trans. Power Electron.* **2018**, *33*, 5401–5414. [[CrossRef](#)]
31. Trinh, Q.; Choo, F.; Tang, Y.; Wang, P. Control Strategy to Compensate for Current and Voltage Measurement Errors in Three-Phase PWM Rectifiers. *IEEE Trans. Ind. Appl.* **2019**, *55*, 2879–2889. [[CrossRef](#)]
32. Dong, L.; Jatskevich, J.; Huang, Y.; Chapariha, M.; Liu, J. Fault diagnosis and signal reconstruction of hall sensors in brushless permanent magnet motor drives. *IEEE Trans. Energy Convers.* **2016**, *31*, 118–131. [[CrossRef](#)]

33. Chakraborty, C.; Verma, V. Speed and current sensor fault detection and isolation technique for induction motor drive using axes transformation. *IEEE Trans. Ind. Electron.* **2015**, *62*, 1943–1954. [[CrossRef](#)]
34. Scelba, G.; De Donato, G.; Pulvirenti, M.; Capponi, F.; Scarcella, G. Hall-effect sensor fault detection, identification, and compensation in brushless DC drives. *IEEE Trans. Ind. Appl.* **2016**, *52*, 1542–1554. [[CrossRef](#)]
35. Diao, S.; Diallo, D.; Laboure, E. A nonlinear observer for DC bus voltage estimation and sensor diagnosis for a battery charger used in automotive systems. In Proceedings of the 2015 IEEE 24th International Symposium on Industrial Electronics (ISIE), Buzios, Brazil, 3–5 June 2015; pp. 438–443.
36. Najafabadi, T.; Salmasi, F.; Jabehdar-Maralani, P. Detection and isolation of speed-, DC-link voltage-, and current-sensor faults based on an adaptive observer in induction-motor drives. *IEEE Trans. Ind. Electron.* **2011**, *58*, 1662–1672. [[CrossRef](#)]
37. Kommuri, S.; Lee, S.; Veluvolu, K. Robust sensors-fault tolerance with sliding mode estimation and control for PMSM drives. *IEEE/ASME Trans. Mechatron.* **2018**, *23*, 17–28. [[CrossRef](#)]
38. Salmasi, F.; Najafabadi, T.; Maralani, J. An adaptive flux observer with online estimation of DC-link voltage and rotor resistance for VSI-based induction motors. *IEEE Trans. Power Electron.* **2010**, *25*, 1310–1319. [[CrossRef](#)]
39. Beng, G.; Zhang, X.; Vilathgamuwa, D. Sensor fault-Resilient control of interior permanent-magnet synchronous motor drives. *IEEE/ASME Trans. Mechatron.* **2015**, *20*, 855–864. [[CrossRef](#)]
40. Teng, Q.; Tian, J.; Duan, J.; Cui, H.; Zhu, J.; Guo, Y. Sliding-mode MRA observer-based model predictive current control for PMSM drive system with DC-link voltage sensorless. In Proceedings of the 2017 20th International Conference on Electrical Machines and Systems (ICEMS), Sydney, Australia, 11–14 August 2017; pp. 1–6.



© 2020 by the authors. Licensee MDPI, Basel, Switzerland. This article is an open access article distributed under the terms and conditions of the Creative Commons Attribution (CC BY) license (<http://creativecommons.org/licenses/by/4.0/>).